Persistent Sputtering Yield Reduction in Plasma-Infused Foams

Gary Z. Li and Richard E. Wirz

Phys. Rev. Lett. **126**, 035001 — Published 22 January 2021

DOI: 10.1103/PhysRevLett.126.035001

Persistent Sputtering Yield Reduction in Plasma-Infused Foams

Gary Z. Li* and Richard E. Wirz†
Plasma & Space Propulsion Laboratory
University of California, Los Angeles, CA 90095, USA
(Dated: December 14, 2020)

Aluminum microfoams are found to exhibit persistent sputtering yield reductions of 40-80% compared to a flat aluminum surface under 100 to 300 eV argon plasma bombardment. An analytical model reveals a strong dependency of the yield on the foam geometry and plasma sheath. For foam pore sizes near or larger than the sheath thickness, the plasma infuses the foam and transitions the plasma-surface interactions from superficial to volumetric phenomena. By defining a plasma infusion parameter, the sputtering behavior of foams is shown to be separated into the plasma-facing and plasma-infused regimes. While plasma infusion leads to a larger effective sputtering area, geometric recapture of ejected particles facilitates an overall reduction in yield. For a given level of plasma infusion, the reductions in normalized yield are more pronounced at lower ion energies since angular sputtering effects enable more effective geometric recapture of sputterants.

At a plasma-material interface, an electric field in the non-neutral plasma sheath accelerates ions to impact the surface [1]. For structured surfaces with features much smaller than the sheath thickness, the planar sheath boundary forms parallel to the macroscopic surface and ions impact local features at oblique incidence angles. At low ion energies ($\lesssim 1$ keV), atoms will be preferentially ejected in the direction of travel relative to the surface normal vector [2]. The forward ejected atoms most likely deposit on nearby surfaces, resulting in a large recapture fraction. The reduced sputtering yield of structured surfaces has been measured for many geometries [3–6], and is beneficial for applications such as nuclear fusion [7] and electric propulsion [8]. Unfortunately, the reduction in yield is only temporary as the surface features ultimately erode away [9, 10]. For a sustained reduction in yield, a volumetrically-structured material, such as an open-cell foam, is required.

An open-cell foam is an interconnected network of pores and ligaments with diameters, D and d, respectively. Given a sheath thickness, L_s, a plasma-facing foam with $D \ll L_s$ has an external planar sheath. Ions accelerated through the sheath impact top-layer ligaments or enter the foam through pores and produce a cascade of internal sputter-deposition events. The ligament network recaptures sputterants and reduces the overall yield. In a transitional regime, $D \sim L_s$, the plasma molds to ligament surfaces and 3D sheath effects alter the local ion flux, incidence angles, and ion-energy distribution [11, 12]. If the pore size is significantly larger than the sheath ($D \gg L_s$), the plasma infuses into the foam volume in a unique regime that the authors define as the plasma-infused regime. In this limit, the sheath forms along ligament surfaces and the 1D sheath theory can again be applied. For the limiting case where $D \gg d \gg L_s$, an ideal plasma-infused foam has a uniform isotropic plasma, with sputtering surfaces throughout the volume; in essence, the bulk plasma-surface interactions are moved from the foam surface to the interior volume.

The plasma-foam sputtering regimes can therefore be defined by introducing a plasma-infusion parameter, $\xi = D/L_s$. Based on the scenarios described in the previous paragraph, the three regimes are the (1) plasma-facing ($\xi \ll 1$), (2) transitional ($\xi \sim 1$), and (3) plasma-infused ($\xi \gg 1$) regimes. The foam sputtering yield is shown to be strongly dependent on the distinct plasma-foam sputtering behavior for each regime.

In this Letter, we present time-dependent measurements of the effective sputtering yield for 10 Pores Per Inch (PPI) and 40 PPI aluminum foams under 100 - 300 eV argon plasma bombardment. The experiments were conducted in the Plasma interactions (Pi) facility at UCLA [9, 13] which consists of a partially ionized argon plasma column with magnetized electrons and unmagnetized ions. The foam samples are negatively biased relative to ground for energetic ion bombardment up to 300 eV, and sputtering yields are measured using a quartz crystal microbalance. More details on the Pi facility can be found in Ref [9].

The 10 PPI and 40 PPI aluminum samples are Duocel foams with 14-faceted polyhedral cells and relative densities ($\rho_{\text{foam}}/\rho_{\text{solid}}$) of 8% . The average pore diameters, D, are calculated from the pore densities to be 1.5 mm and 380 µm for 10 PPI and 40 PPI foams respectively while the average ligament diameters, d, are found to be 415 µm and 112 µm. The 21.3 mm diameter disks are installed in Macor mounts with solid aluminum backplates. Sample cleaning to remove surface impurities and round sharp edges was achieved using a brief plasma exposure.

To investigate relative sputtering behavior, the foam samples are exposed to argon plasma with a centerline plasma density of $n_e = 10^{17}$ m^{-3} and an electron temperature of $T_e = 5$ eV as measured by a Langmuir probe. For negative-going cathode sheaths with a sufficiently large potential drop ($\Delta\phi_s \gg T_e$), the Child-Langmuir law gives a sheath thickness of $L_s/\lambda_D = \sqrt{2}/3(2e\Delta\phi_s/T_e)^{3/4}$, where $\lambda_D^2 = \epsilon_0 k_B T_e/n_e e^2$ is the Debye length and $\Delta\phi_s$ is the potential difference

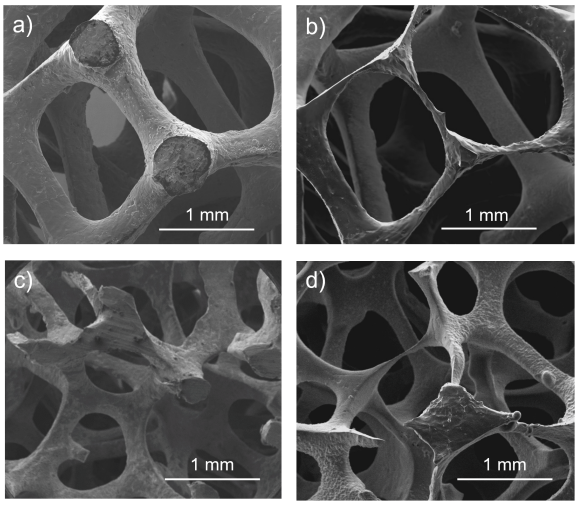

FIG. 1. SEM images show the 10 PPI foam a) before and b) after plasma exposure and the 40 PPI foam c) before and d) after plasma exposure. Images are taken at 4.3 mm and 10 mm from the plasma exposure center for the 10 and 40 PPI foams, respectively.

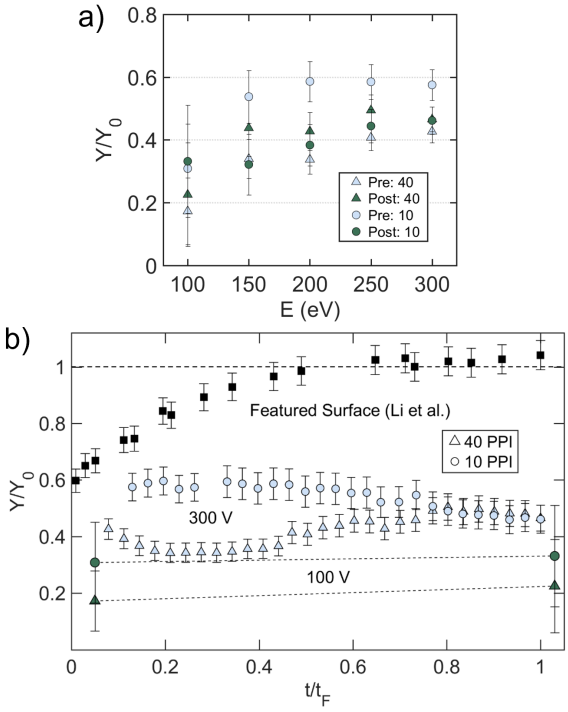

FIG. 2. a) The sputtering yields for 10 PPI and 40 PPI aluminum foams normalized by the flat aluminum yields[16] before and after the 30 h, 300 eV exposure. b) The time-dependent yields with micro-featured molybdenum data from Li et al. [9]. The normalizing values are $t_F = 30$ h and $Y_0 = 0.5$ atoms/ion for the aluminum foam and $t_F = 18$ h and $Y_0 = 0.41$ atoms/ion for the molybdenum data.

between the plasma and the wall [14, 15]. For this plasma, $\lambda_D = 50$ µm and L_s ranges from 375 to 855 µm for $\Delta\phi_s = 100$ to 300 V, which were examined at increments of 50 V. The range of plasma-infusion parameters for each foam is then $\xi_{10} = D/L_s = 6.8$ to 3.0 and $\xi_{40} = 1.7$ to 0.7 for $\Delta\phi_s = 100$ to 300 V, respectively. The 10 PPI foam is within the plasma-infused regime, while the 40 PPI foam is in the transitional regime with partially plasma-infused characteristics. The background neutral pressure, $P_o = 2.7 \times 10^{-2}$ Pa, gives a mean free path of $\lambda_{\rm mfp} = 1.7$ m at room temperature. Since $\lambda_{\rm mfp} \gg L_s$, the sheaths in this experiment are assumed to be collisionless.

Figure 1a-1d show Scanning Electron Microscope (SEM) images of the 10 PPI and 40 PPI foams before and after plasma exposure at calibrated positions. The general structure for the 10 PPI foam remains the same after ion bombardment but the ligaments in the outermost layer are clearly eroded. Although $\xi_{10} > 1$ predicts that the foam is in the plasma-infused regime, the 2nd layer appears largely unchanged after plasma exposure. $\xi_{10} = 3.0$ may be insufficient for plasma-infusion beyond the 1st layer. The 40 PPI foam shows large discrepancies between the before and after images, indicating that multiple layers were removed.

Effective sputtering yields were measured at ion energies of 100 – 300 eV before and after the long duration exposure as shown in Figure 2a. The 40 PPI yields appear to increase slightly after exposure, while the 10 PPI yields decrease by as much as 20%. The erosion of multiple layers in the 40 PPI foam may explain the minimal change in yield post-exposure while the single layer ligament thinning for the 10 PPI foam explains the larger decrease in yield at all but the 100 eV data point. The most significant observation is the larger reduction in yield at lower energies, as much as 80% and 70% for the 40 and 10 PPI foams, respectively. At 100 eV, sputtering occurs closer to the threshold energy where the angular sputtering profiles are preferentially oriented to decrease the overall yield.

The time-dependent yields of the 10 PPI and 40 PPI foams under continuous 300 eV Ar^+ bombardment are shown in Figure 2b with normalized axes. Sputtering yields for a featured molybdenum surface are included from Li et al. to show the characteristic approach to flat yield as features are eroded away [9]. In contrast, it is shown for the first time that foam can maintain a persistent reduction in sputtering yield compared to a flat surface. The 10 PPI yield begins at 0.60 and decreases to 0.45 as the top-layer ligaments are thinned as observed in Figure 1. Meanwhile, the 40 PPI yield starts with a lower yield of 0.40 and shows cyclic behavior with oscillations up to ±0.10 about the mean value. The cyclic yield curves are a function of the self-similar foam geometry and have time-scales related to the thickness of the ligaments. A simple thickness erosion calculation using

300 eV ions, a flat aluminum yield of 0.5 atoms/ion, and an ion flux of 2×10^{17} ions cm^{-2} s^{-1} yields characteristic ligament erosion times of 7 h and 2 h for 10 PPI and 40 PPI foams, respectively. Based on order of magnitude, the 10 PPI foam will have roughly one layer eroded, while the 40 PPI foam will have multiple layers removed during exposure. With a longer test duration, the 10 PPI foam is also expected to display oscillatory yields. In Figure 2b, over normalized time, the two curves appear to converge. However, the 100 V data doesn't show the same trend, indicating the convergence is likely coincidental. Nevertheless, the observation merits further investigation with longer test durations and computational analysis. In the following discussion, the experimental observations are analyzed in the context of an analytical plasma-foam sputtering model.

Plasma-foam sputtering includes competing mechanisms that can reduce or increase the sputtering yield compared to a flat surface, including material opacity, effective sputtering area, ballistic deposition, and plasma density gradients. The following analytical relationship was derived to capture these effects:

$$Y = Y_0 \sum_{k=1}^{N} (1 - p^{(k)}) f_A^{(k)} f_\beta^{(k)} (1 - f_{\text{dep}}^{(k)}) f_{\nabla n}^{(k)}, \quad (1)$$

where $p^{(k)}$ is the open area fraction of the k^{th} layer, $f_A^{(k)}$ is the ratio of the sputtering area compared to a flat surface, $f_\beta^{(k)}$ is the backsputter factor, $f_{\text{dep}}^{(\text{k})}$ is the deposition factor, and $f_{\nabla n}^{(k)}$ is the plasma density gradient effect. The first layer exposed to plasma, given by $k = 1$, has $Y = Y_0(1 - p^{(1)}) f_A f_\beta$ where $f_{\text{dep}}^{(1)} = 0$. The effective yield reduces to $Y = Y_0$ when the material becomes fully opaque, the surface is flat, and all particles are backsputtered. The plasma-gradient term, which will be discussed later, is only applicable for a plasma-infused foam and allows for decreases in subsurface ion flux to be assessed.

A 3D cage structure with pore size, D, and cylindrical struts with diameter, d, is used to represent a simplified foam geometry [17]. Based on symmetry, the following parameters can be calculated with 2D approximations to effectively represent a 3D foam. The material opacity represents the fraction of a planar layer occupied by sputtered ligaments. The material opacity is defined as $1 - p^{(k)}$ where $p^{(k)}$ is the open area fraction of a single pore. Each pore is assumed to have identical open area fractions, and the sublayers are arranged such that the sputtering area is maximized. For $d \ll D$, the open area fraction is approximately $p^{(k)} = 1 - 2d/D$, and the material opacity is $1 - p^{(k)} = 2d/D$.

The effective sputtering area is given by $f_A f_\beta$ and describes the ratio of ligament area that results in backsputtered atoms compared to a flat surface. The area factor is dependent on the plasma-foam sputtering regime. In the plasma-facing regime, the ions see a cylindrical ligament projected as a flat plane so $f_A = 1$. For plasma-infused foams, the entire ligament is sputtered so $f_A = \pi$.

The backsputter factor, f_β, is calculated by determining the average fraction of sputterants ejected upstream for a single ligament. The angular sputtering profile for low energy heavy ions is given by

$$S(E, \theta, \theta_1) \propto \cos\theta_1 \left[1 - \frac{1}{4}\sqrt{\frac{E_{\text{th}}}{E}} \times \left(\cos\theta\gamma(\theta_1) + \frac{3}{2}\pi \sin\theta \sin\theta_1 \cos\phi_1\right)\right] \quad (2)$$

where $\gamma(\theta_1)$ is a monotonic function defined in Ref. [18], E is the ion energy, θ is the ion incidence angle, θ_1 is the sputterant ejection angle, ϕ is the azimuthal ejection angle, and E_{th} is the sputtering threshold energy [18, 19]. The angular sputtering profile in a 2D plane is found by taking $\phi = 0$ and $\phi = \pi$. For plasma-infused foams, the ions will be normally incident on ligaments, giving a symmetric undercosine sputtering profile and $f_\beta = 0.5$. In the plasma-facing regime, the ions will hit the ligament at oblique incidence angles ranging from $\theta = 0°$ at the center to $\theta = 90°$ at the edge. Two example cases are shown in Figure 3b. At glancing incidence, the oblique yield increases up to a critical angle and decreases to zero at 90°. Here, the increased oblique yield is included as a weighting term on the local f_β^* as $f_\beta = f_\beta^* \times Y_{\text{oblq}}/Y_0$, where $Y_{\text{oblq}}/Y_0 = 1/\cos^n\theta$ for $0 < \theta < \theta_c$ and 0 for $\theta > \theta_c$. n and θ_c depend on the ion energy and surface roughness. The following analysis uses $n = 1$ and $\theta_c = 80°$ based on Ref [20]. f_β is calculated from the average of $f_{\beta,i}$ for uniformly discretized ion impacts along the ligament.

The deposition factor captures the essence of sputtering yield reduction via geometric structuring. In a foam, the ligaments are both the source of sputtering and the obstructions for deposition. A simple model uses a sputtering point source at the origin and a 2D array of self-similar circular ligament cross-sections as illustrated in Figure 3a. The sputterant emission is assumed to be uniform with angle and the mean free path is much larger than the domain. A numerical model integrates through a discretized number of particles, layers, and ligaments, and determines the fraction of sputterants that intersect other ligaments in the array.

The effective sputtering yield can be simplified to

$$\frac{Y}{Y_0} = \sum_{k=1}^{N} \frac{2d_k}{D_k} f_A^{(k)}(\xi) f_\beta^{(k)}(E, \xi) \left[1 - f_{\text{dep}}^{(k)}\left(\frac{d_k}{D_k}\right)\right] f_{\nabla n}^{(k)} \quad (3)$$

where the key dependencies are the ligament-pore size ratio d/D, ion energy E, and the plasma-infusion parameter ξ. Equation 3 is used to analyze the observations from the experiment.

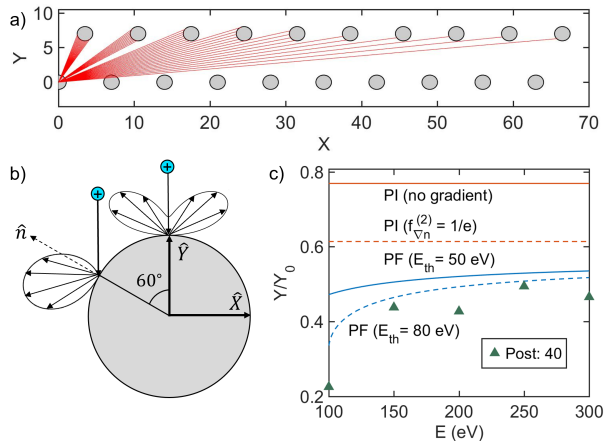

FIG. 3. a) An illustration of the deposition domain for $d/D = 1/6$ with 100 particles, 10 ligaments, and 2 layers for ion collisions with a ligament at position (0,0). b) Angular sputter profiles for two ion incidence angles (e.g. in the plasma-facing case). c) Sputtering yields for plasma-facing (PF) foams calculated with two E_{th} values, plasma-infused (PI) foams with and without a plasma gradient where $f_{\nabla n}^{(2)} = n_e^{(2)}/n_e^{(1)} = 1/e$, and the post-exposure 40 PPI foam.

In Figure 2c, the 10 PPI yield at 300 eV was shown to be initially larger than the 40 PPI yield. The ratio d/D is nearly 1/6 for both 10 PPI and 40 PPI foams, indicating that the two foams are geometrically self-similar. Since the ion energy is also identical for both tests, Equation 3 suggests the difference in yield stems from the plasma-infusion parameter, ξ. Recall that the parameters $\xi_{10} = 3.0$ and $\xi_{40} = 0.7$ imply that the 10 PPI and 40 PPI foams are in the plasma-infused and transitional regimes, respectively. Equation 3 is solved using a 2-layer approximation and assuming the limit where the 10 PPI and 40 PPI foams are fully plasma-infused and fully plasma-facing, respectively. The calculated yields are $Y^{(10)}/Y_0 = 0.77$ and $Y^{(40)}/Y_0 = 0.53$ with the ratio being $Y^{(10)}/Y^{(40)} = f_A^{(10)} f_\beta^{(10)} / f_A^{(40)} f_\beta^{(40)} = 1.44$. The yield ratio shows good agreement with the initial measured ratio of 1.5. The 10 PPI yield is larger than the 40 PPI yield due to the larger effective sputtering area, $f_A f_\beta$, resulting from higher plasma infusion of the ligaments. In general, this analysis reveals that a foam with a larger plasma-infusion parameter will have a larger yield than a self-similar foam at the same ion energy. Moreover, for a given energy, a fully plasma-infused foam defines an upper bound for the effective sputtering yield while a plasma-facing foam defines the lower bound.

An analysis of the time evolution can be conducted based on the thinning of top-layer ligaments observed for the 10 PPI foam in Figure 1. The scenario can be described with a 2-layer approximation and a hybrid approach where the 1st layer is plasma-infused and the 2nd layer is plasma-facing. The initial ligament diameter is measured to be $d^i = 364$ µm, which decreases by $\Delta d = 270$ µm, leading to final foam dimensions of $d_1^f = 94$ µm and $D_1^f = D_1^i + \Delta d = 2.81$ mm. The 2nd layer is assumed to be unchanged. Equation 3 is solved for the effective yields and can be divided into layer-specific contributions, δY_1 and δY_2. The initial yield is $Y^i/Y_0 = 0.61$ with components $\delta Y_1^i = 0.45$ and $\delta Y_2^i = 0.16$. The final yield is $Y^f/Y_0 = 0.36$ with $\delta Y_1^f = 0.10$ and $\delta Y_2^f = 0.26$. The yield contribution from the 1st layer decreases due to reduced material opacity from thinner ligaments while the contribution from the 2nd layer increases due to a lower deposition factor. The overall yield decreases from 0.61 to 0.36 indicating that the total yield is more dependent on material opacity than effective trapping due to pore size. The model predictions agree with experimental results which showed a reduction in yield from 0.60 to 0.45.

Finally, the larger reduction in yield at lower ion energies measured in Figure 2b can be investigated. Physically, the yield depends on how the effective sputtering area changes with plasma-infusion parameter, ξ, and the energy-dependent angular sputtering profiles, $S(E, \theta, \theta_1)$. In Figure 3c, the yields for plasma-facing foams ($\xi \gg 1$) are shown to decrease with lower ion energy and also depend strongly on E_{th} because this threshold energy is a function of incidence angle and alters the shape of the angular sputtering profiles [21]. $E_{\text{th}} = 50$ eV was determined for $Ar^+ \rightarrow$ Al based on extrapolation of best-fit angular profiles with similar ion-atom combinations and energy levels [4]. The observed trend is successfully predicted by changing angular profiles with lower ion energy.

However, the 10 PPI and 40 PPI foams have $\xi \geq 1$ and should exhibit partially plasma-infused behavior. In this case, one should account for a negative plasma density gradient into the foam. The $f_{\nabla n}^{(k)}$ term allows for a decreased contribution from layer k based on a lower plasma density relative to upstream layers. A control volume analysis of plasma flux attenuation into the foam shows that the plasma density should decay exponentially with an e-folding decay length, δ, of $\mathcal{O}(D^2/d)$. For a fully plasma-infused foam with $D \gg d \gg L_s$, δ is much greater than D so the plasma density gradient is negligible. However, for a partially plasma-infused foam $d \rightarrow d_{\text{eff}}$, where $d_{\text{eff}} = d + 2L_s$ is the effective diameter of the sheath surrounding each ligament. Given that sheath boundaries for two adjacent ligaments must not overlap to maintain a quasineutral plasma, $d_{\text{eff}} = D$ in the large sheath limit. Therefore, $\delta \sim D$ and the density gradient for a 2-layer foam yields a ratio of plasma densities, $f_{\nabla n}^{(2)} = n_e^{(2)}/n_e^{(1)} = 1/e$, where $n_e^{(k)}$ is the bulk plasma density at the k^{th} layer. Figure 3c shows the yield for a fully plasma-infused foam and a partially plasma-infused foam with $f_{\nabla n}^{(2)} = 1/e$. This plot illustrates the effect of decreased subsurface ion density, and hence ion flux, on the overall sputtering yield.

In conclusion, we have experimentally demonstrated the persistent sputtering yield reduction of aluminum foams and described the sputtering behavior across plasma-infusion regimes. Analytical modeling reveals that the reduction in yield is a consequence of geometric effects, angular sputtering distributions, and plasma gradients in plasma-infused foams. By normalizing the yield, the results can be extended beyond aluminum to other materials. We define a plasma infusion parameter, ξ, to separate the behavior of plasma-facing and plasma-infused foams into two notably distinct regimes, while the transitional regime shares properties of the two limits. Furthermore, the unique characteristics of reduced sputtering and volumetric plasma-surface interaction motivates the categorization of plasma-infused foams as a new multi-phase material. Future studies can further characterize the sputtering behavior in the plasma-infused regime, and identify the influence of additional effects such as power losses to the walls, plasma density profiles, and the 3D plasma sheath.

The authors would like to acknowledge Max Hegglin, Angelica Ottaviano, Anirudh Thuppul, and Adam Collins for their contributions. Funding was provided by the National Defense Science and Engineering Graduate Fellowship and the Air Force Office of Scientific Research Award No. FA9550-14-10317 (UCLA Subaward No. 60796566-114411).

* g.li@ucla.edu
† wirz@ucla.edu

[1] N. Hershkowitz, Sheaths: More complicated than you think, Physics of Plasmas **12**, 1 (2005).
[2] U. Littmark and W. O. Hofer, The influence of surface structures on sputtering: Angular distribution and yield from faceted surfaces, Journal of Materials Science **13**, 2577 (1978).
[3] D. Rosenberg and G. K. Wehner, Sputtering Yields for Low Energy He+-, Kr+-, and Xe+-Ion Bombardment, Journal of Applied Physics **33**, 1842 (1962).
[4] C. E. Huerta, T. S. Matlock, and R. E. Wirz, View factor modeling of sputter-deposition on micron-scale-architectured surfaces exposed to plasma, J. Appl. Phys. **113303**, 1 (2016).
[5] G. K. Wehner and D. J. Hajicek, Cone formation on metal targets during sputtering, Journal of Applied Physics **42**, 1145 (1971), arXiv:1310.0502.
[6] T. Abe, K. Obara, H. Nakamura, K. Sone, H. Ohtsuka, R. Yamada, M. Saidoh, and M. Shimizu, Reduction of effective sputtering yield by honeycomb structures, Journal of Nuclear Science and Technology **15**, 471 (1978).
[7] R. Behrisch, J. Roth, G. Staudenmaier, and H. Verbeek, Sputtering in Fusion Devices, Nuclear Instruments and Methods in Physics Research Section B: Beam Interactions with Materials and Atoms **18**, 629 (1987).
[8] R. M. Myers, N. Suzuki, A. J. Kelly, and R. G. Jahn, Cathode phenomena in a low-power magnetoplasmadynamic thruster, Journal of Propulsion and Power **7**, 760 (1991).
[9] G. Z. Li, T. S. Matlock, D. M. Goebel, C. A. Dodson, C. S. R. Matthes, N. M. Ghoniem, and R. E. Wirz, In situ plasma sputtering and angular distribution measurements for structured molybdenum surfaces, Plasma Sources Science and Technology **26** (2017).
[10] C. S. Matthes, N. M. Ghoniem, G. Z. Li, T. S. Matlock, D. M. Goebel, C. A. Dodson, and R. E. Wirz, Fluence-dependent sputtering yield of micro-architectured materials, Applied Surface Science **407**, 223 (2017).
[11] C. K. Kim and D. J. Economou, Plasma molding over surface topography: Energy and angular distribution of ions extracted out of large holes, Journal of Applied Physics **91**, 2594 (2002).
[12] D. Kim and D. J. Economou, Simulation of plasma molding over a ring on a flat surface, Journal of Applied Physics **94**, 3740 (2003).
[13] T. S. Matlock, D. M. Goebel, R. Conversano, and R. E. Wirz, A dc plasma source for plasmamaterial interaction experiments, Plasma Sources Science and Technology **23**, 025014 (2014).
[14] C. D. Child, Discharge from hot CaO wires, Science **32**, 492 (1911).
[15] I. Langmuir, The interaction of electron and positive ion space charges in cathode sheaths, Phys. Rev. **33**, 954 (1929).
[16] Y. Yamamura and H. Tawara, Energy dependence of ion-induced sputtering yields from monatomic solids at normal incidence, Atomic Data and Nuclear Data Tables **62**, 149 (1996).
[17] C. E. Huerta, M. I. Patino, and R. E. Wirz, Secondary electron emission from textured surfaces, Journal of Physics D: Applied Physics **51**, 10.1088/1361-6463/aab1ac (2018).
[18] Z. L. Zhang and L. Zhang, Anisotropic angular distribution of sputtered atoms, Radiation Effects and Defects in Solids **159**, 301 (2004).
[19] Y. Yamamura, Contribution of Anisotropic Velocity Distribution of Recoil Atoms To Sputtering Yields and Angular Distributions of Sputtered Atoms., Radiation effects **55**, 49 (1981).
[20] T. A. Cassidy and R. E. Johnson, Monte Carlo model of sputtering and other ejection processes within a regolith, Icarus **176**, 499 (2005).
[21] Q. Wei, K. D. Li, J. Lian, and L. Wang, Angular dependence of sputtering yield of amorphous and polycrystalline materials, Journal of Physics D: Applied Physics **41**, 10.1088/0022-3727/41/17/172002 (2008).